Optics & Laser Technology 188 (2025) 112858

Contents lists available at ScienceDirect

Optics and Laser Technology

journal homepage: www.elsevier.com/locate/optlastec

Full length article

Assembling magneto-optical heterostructures for all-optical multi-functional devices

Jie Xu [a,*], Yun You [b], Sanshui Xiao [c], Lujun Hong [d], Yun Shen [d], Kosmas L. Tsakmakidis [e,*], Yamei Luo [a,*]

[a] School of Medical Information and Engineering, Southwest Medical University, Luzhou 646000, China
[b] School of Science, East China Jiaotong University, Nanchang 330013, China
[c] DTU Electro, Department of Electrical and Photonics Engineering, Technical University of Denmark, DK-2800, Kgs. Lyngby Denmark
[d] Institute of Space Science and Technology, Nanchang University, Nanchang 330031, China
[e] Section of Condensed Matter Physics Department of Physics, National and Kapodistrian University of Athens, Panepistimioupolis, Athens GR-157 84, Greece

ARTICLE INFO

Keywords:
YIG
Logic gates
One-way edge modes
All-optical devices
Filter
Splitter

ABSTRACT

All-optical computing has recently emerged as a vibrant research field in response to the energy crisis and the growing demand for information processing. However, the efficiency of subwavelength-scale all-optical devices remains relatively low due to challenges such as back-scattering reflections and strict surface roughness. Furthermore, achieving multifunctionality through the reassembly of all-optical structures has thus far been rarely accomplished. One promising approach to address these issues is the utilization of one-way edge modes. This work proposes four types of deep-subwavelength ($\sim 10^{-2}\lambda_0$, where λ_0 is the wavelength in vacuum) all-optical functional devices based on yttrium iron garnet (YIG): a phase modulator, a filter, a splitter, and logic gates. These devices are based on robust one-way edge modes and/or index-near-zero (INZ) modes but do not require an external magnetic field, which can allow for flexible assembly. In particular, a phase modulation range spanning from $-\pi$ to π, a perfect filter that divides the input port's one-way region into two output one-way regions with equal bandwidth, a multi-frequency splitter with an equal splitting ratio (e.g., 50/50), and self-consistent logic gates relying on INZ modes are investigated. Our findings may find applications in compact optical calculations and integrated optical circuits.

1. Introduction

Optical communication is known for its low loss [1], parallel calculation capability [2], and high speed. As a result, all-optical devices are attracting increasing attention. Regular all-optical devices include, but are not limited to, optical filters, sensors, splitters, switches, frequency/phase/amplitude modulators, couplers, and amplifiers. Most of these devices rely on the electro-optic (EO) effect, thermo-optic (TO) effect, or nonlinear optical (NLO) effect. Among these optical effects, the linear EO effect has been extensively studied in fields such as optical sensing and optical frequency combs [3] due to its ultrafast response [4]. The TO effect is commonly employed in the design of optical switches [5], while the NLO effect is primarily used for light control with light, enabling applications such as laser generation and optical switching [6]. However, all-optical devices based on EO, TO, or NLO suffer from high power consumption due to reflection induced by reciprocity/symmetry and fabrication errors.

In recent years, there has been a significant focus on one-way edge modes due to their potential for breaking the diffraction limit (similar to SPPs) [7–9], robust processing/computing capabilities [10], and low loss. One common approach to achieve one-way edge modes is by utilizing photonic crystals (PhCs). The key lies in engineering a special surface that is bounded by materials with zero and nonzero Chern numbers. According to the bulk-edge correspondence [11,12], this ensures the existence of one-way edge mode(s) on this surface. The robustness of one-way modes in PhCs to imperfections or bends has been proposed theoretically and verified experimentally by several groups [13–15]. The topologically protected edge modes in PhCs have been suggested for realizing a variety of functional devices such as splitters [16], filters [17], circulators [18], and phase modulators [19]. However, PhCs still pose challenges in terms of their relatively complex manufacturing process and the large device size compared to the wavelength of the guiding wave (λ_0). This poses a challenge for achieving subwavelength or even deep/ultra-subwavelength optical devices.

---

[*] Corresponding authors.
E-mail addresses: xujie@swmu.edu.cn (J. Xu), ktsakmakidis@phys.uoa.gr (K.L. Tsakmakidis), luoyamei@swmu.edu.cn (Y. Luo).

https://doi.org/10.1016/j.optlastec.2025.112858
Received 19 December 2024; Received in revised form 2 March 2025; Accepted 21 March 2025

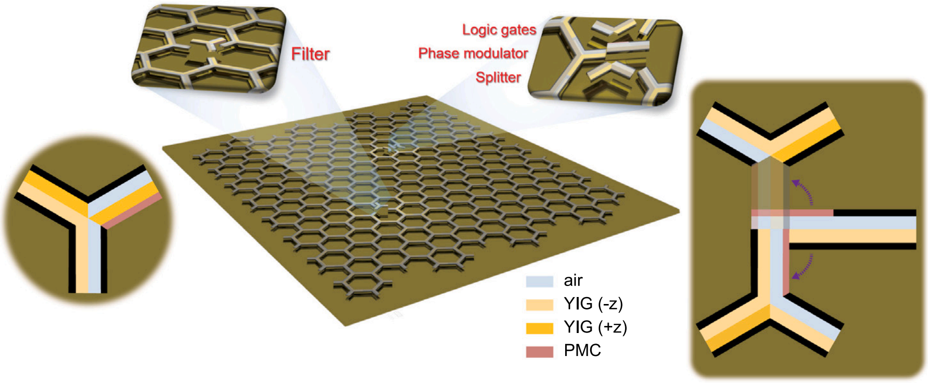

Fig. 1. Assembled all-optical communication systems and functional devices utilizing YIG with remanence, along with PEC and PMC walls.

Recently, our group has proposed several subwavelength magneto-optical (MO) one-way structures and discovered interesting phenomena/devices, such as unidirectional/bidirectional slow wave [20,21], a perfect optical buffer with zero phase shift [22], and all-optical logic gates (LGs) [23]. The most significant advantage of the MO one-way structure is its extremely simple manufacturing process, requiring only two joint layers and not having strict requirements for surface roughness. Ultra-subwavelength all-optical devices can be achieved based on the MO structure, regardless of the nonlocal effect, which holds true in common scenarios, especially when the wavenumber is relatively small (e.g., $k < 100k_0$) [24,25].

Here, we propose several intriguing deep-subwavelength ($\sim 10^{-2}\lambda_0$) all-optical microwave functional devices, including a phase modulator, a filter, a splitter, and self-consistent LGs. These devices are based on assembling MO structures consisting of yttrium iron garnet (YIG) with remanence. We study the propagation characteristics of surface magnetoplasmons (SMPs) [26] in theory, and demonstrate the low-loss properties of one-way SMPs through full-wave numerical simulations. Furthermore, we verify the functionality of these all-optical devices. The key to realizing the all-optical phase modulator, splitter, and self-consistent LGs lies in the utilization of one-way INZ modes. Unlike other INZ modes found in epsilon-near-zero (ENZ) [27–29], mu-near-zero (MNZ) [30], or epsilon-and-mu-near-zero (EMNZ) [31] metamaterials, the INZ modes in our work exhibit a single propagation direction and can be easily adjusted within a continuous band.

2. Tunable INZ modes and all-optical phase modulator

YIG stands out as one of the most captivating MO materials, finding widespread applications in optical communication. These applications encompass optical isolators [32,33], band-pass filters [34], high-efficiency optomagnonic micron-sized resonators [35], robust LGs [23], and more. Benefiting from the unique magnetization characteristics of YIG, residual magnetism persists even after removing the bias magnetic field. This property holds great potential for the realization of reliable all-optical communication, as depicted in Fig. 1. In this paper, we demonstrate that by utilizing YIG with remanence and perfect magnetic conductor (PMC) walls, a wide range of all-optical functional devices, including phase modulators, filters, splitters, and LGs, can be achieved. Importantly, these devices can be finely controlled and integrated into a system, as illustrated in Fig. 1.

To investigate the impact of PMC walls on SMPs, we first construct four MO heterostructures surrounded by PEC and/or PMC walls [36]. These structures are named as follows: the PEC-air-YIG-PEC (EDYE) structure, the PEC-air-YIG-PMC (EDYM) structure, the PMC-air-YIG-PEC (MDYE) structure, and the PMC-air-YIG-PMC (MDYM) structure, as illustrated in the inset pictures in Fig. 2. It should be noted that the YIG material with remanence are used in this study, which means that all the proposed functional devices in this work do not require precise control of an external magnetic field. Our theoretical analysis reveals the following forms for the dispersion relationship of these structures:

$$\alpha_{\mathrm{r}} X_1 + \frac{\mu_{\mathrm{r}2}}{\mu_{\mathrm{r}1}} k - \alpha_{\mathrm{d}} \mu_{\mathrm{vr}} X_2 = 0 \tag{1}$$

where X_1 and X_2 are parameters that directly depend on the lower and upper boundary conditions of the structures, respectively. For the four structures, their values are as follows:

$$\text{Lower boundary} \begin{cases} X_1 = \dfrac{1}{\tanh(\alpha_{\mathrm{r}} d_2)} & \text{(PEC)} \\[2ex] X_1 = \dfrac{\alpha_{\mathrm{r}} \cdot \tanh(\alpha_{\mathrm{r}} d_2) - \frac{\mu_{\mathrm{r}2}}{\mu_{\mathrm{r}1}} k}{\alpha_{\mathrm{r}} - \frac{\mu_{\mathrm{r}2}}{\mu_{\mathrm{r}1}} k \cdot \tanh(\alpha_{\mathrm{r}} d_2)} & \text{(PMC)} \end{cases} \tag{2}$$

$$\text{Upper boundary} \begin{cases} X_2 = -\dfrac{1}{\tanh(\alpha_{\mathrm{d}} d_1)} & \text{(PEC)} \\[1ex] X_2 = -\tanh(\alpha_{\mathrm{d}} d_1) & \text{(PMC)} \end{cases} \tag{3}$$

where $\mu_{\mathrm{r}1} = 1 + i\frac{\nu\omega_{\mathrm{r}}}{\omega(1+\nu^2)}$ and $\mu_{\mathrm{r}2} = -\frac{\omega_{\mathrm{r}}}{\omega(1+\nu^2)}$ are the nondiagonal elements of the tensor relative permeability of the YIG layers [7,37]. α_{r} and α_{d} represent the attenuation factors of the surface wave in the YIG layer and air, respectively [38]. d_1 and d_2 are the thicknesses of the air and YIG layers. $\omega_{\mathrm{r}} = \mu_0 \gamma M_{\mathrm{r}}$ and $\omega_{\mathrm{m}} = \mu_0 \gamma M_{\mathrm{s}}$. γ, M_{r}, and M_{s} indicate the gyromagnetic ratio, the residual magnetization and the saturation magnetization, respectively. In this paper, we assume $4\pi M_{\mathrm{s}} \approx 1780$ G and $4\pi M_{\mathrm{r}} \approx 1281$ G ($M_{\mathrm{r}} < M_{\mathrm{s}}$) [39,40], inducing $\omega_{\mathrm{m}} = 2\pi f_{\mathrm{m}} = 2\pi \times 5 \times 10^9$ rad/s and $\omega_{\mathrm{r}} = 2\pi \times 3.587 \times 10^9$ rad/s. We emphasize that, despite potential slight variations in remanence in practical scenarios, the theory proposed in this paper remains feasible. Any necessary adjustments would likely be minor, primarily involving corrections to the corresponding operating bands for the devices. Besides, the remanence of YIG can be tuned through doping or heating [41].

In Eqs. (2) and (3), it can be observed that as $k \to \pm\infty$, $X_1 \to 1$ and $X_2 \to -1$. Additionally, Eq. (1) tends to

$$\begin{cases} 1 + \frac{\mu_{\mathrm{r}2}}{\mu_{\mathrm{r}1}} + \mu_{\mathrm{vr}} = 0 \iff \omega_{\mathrm{sp}}^{+} = \omega_{\mathrm{r}} & (k \to +\infty) \\[1ex] -1 + \frac{\mu_{\mathrm{r}2}}{\mu_{\mathrm{r}1}} - \mu_{\mathrm{vr}} = 0 \iff \omega_{\mathrm{sp}}^{-} = 0.5\omega_{\mathrm{r}} & (k \to -\infty) \end{cases} \tag{4}$$

According to Eq. (4), we can expect, at most, one asymptotic frequency for $k > 0$, denoted as ω_{sp}^{+}, and one asymptotic frequency for $k < 0$, denoted as ω_{sp}^{-}. Fig. 2 illustrates the four dispersion curves of SMPs in these structures as $d_1 = d_2 = 0.03\lambda_{\mathrm{m}}$ ($\lambda_{\mathrm{m}} = 2\pi c/\omega_{\mathrm{m}} = 60$ mm). Interestingly, when the lower PEC wall in the original EDYE structure is replaced with a PMC wall (see Fig. 2(b)), the one-way region abruptly changes from the higher region, $\omega_{\mathrm{sp}}^{-} < \omega < \omega_{\mathrm{sp}}^{+}$ (see Fig. 2(a)), to the lower region, $0 < \omega < \omega_{\mathrm{sp}}^{-}$, and simultaneously the propagation direction changes oppositely. Similarly, when the upper PEC wall in the EDYE structure is replaced with a PMC wall (Fig. 2(c)), the asymptotic frequencies and the one-way region remain the same, but the one-way SMPs consistently have positive values of k, i.e., $k > 0$. Furthermore, when both the upper and lower PEC walls are replaced by PMC walls

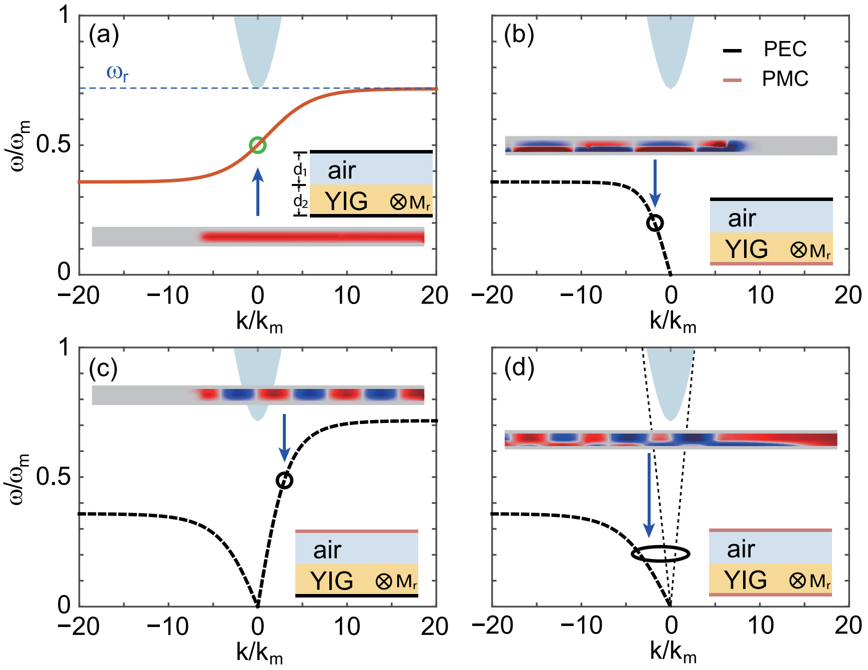

Fig. 2. Dispersion diagrams of 'XDYX' structures where the first 'X' can be either (a, b) PEC or (c, d) PMC, while the second 'X' can also be either (a, c) PEC or (b, d) PMC. The red line and black dashed lines represent the dispersion curves of the SMPs. The cyan dashed area is the bulk zone of the bulk YIG. The insets illustrate the electric-field distributions obtained through finite element method (FEM) simulations. The operating frequencies are indicated by arrows, and a distinct one-way propagation is observed in the insets of (a)–(c). However, only the electric field in the first simulation exhibits a near-zero phase shift, indicating the presence of the INZ mode. The other parameters are $d_1 = d_2 = 0.03\lambda_m$, $\omega_r = 0.7174\omega_m$, and $\varepsilon_d = 1$.

(Fig. 2(d)), the one-way region is completely disrupted due to the emergence of modes based on total internal reflection (TIR).

In the inset of Fig. 2, we present simulation results with a setting of $\nu = 10^{-3}$, which shows good agreement with our theoretical analysis considering lossless materials ($\nu = 0$). The corresponding transmission coefficients in these simulations are approximately 62.20% (effective propagation length $L_{\text{eff}} \simeq 1.63\lambda_0$), 87.73% ($L_{\text{eff}} \simeq 2.17\lambda_0$), and 86.82% ($L_{\text{eff}} \simeq 5.06\lambda_0$). Thus, the proposed deep-subwavelength structures exhibit truly low loss.

Furthermore, one of the most significant differences between Fig. 2(a) and Fig. 2(b,c) is the presence of an INZ mode, marked by a green circle in Fig. 2(a). In our previous work, we proposed a method to control the thickness parameters in order to adjust the INZ modes in magnetized-YIG systems. Similarly, in the current study, we can employ the same approach to achieve tunable INZ modes. The advantage of integrability in this system is undeniable compared to previous systems.

In Fig. 3, we investigate the impact of the thicknesses of YIG (d_2) and air (d_1) on the INZ modes in two cases. In the first case, we assume $d_1 = d_2$ ($< 0.1\lambda_m$, subwavelength). As shown in Figs. 2(a) and 2(b), when we increase d_1, the INZ frequency gradually decreases and remains close to $\omega = 0.5\omega_m$. The red line in Fig. 3(a) represents a fitting curve with the following form:

$$\bar{\omega} = 5.4848 \cdot \bar{d}_1^{\,2} - 0.09412 \cdot \bar{d}_1 + 0.5085 \tag{5}$$

where $\bar{\omega} = \omega/\omega_m$ and $\bar{d}_1 = d_1/\lambda_m$ ($\lambda_m = 2\pi c/\omega_m$). Eq. (5) allows us to estimate the INZ frequency (f_{INZ}) in the $d_1 = d_2$ case. For example, when $d_1 = 0.045\lambda_m$, according to Eq. (5), the INZ frequency should be approximately $0.4932\omega_m$. The inset of Fig. 3(a) further confirms that when $d_1 = d_2 = 0.045\lambda_m$, a point source with $f = 0.4932f_m$ can excite SMPs with a sufficiently large effective wavenumber (k_{eff}) and exhibit no phase shift during propagation. In the second case, we assume $d_2 = 2d_1$. Similar to the first case, we plot f_{INZ} as a function of d_1 in Fig. 3(c). The corresponding fitting equation is as follows:

$$\bar{\omega} = 102.45 \cdot \bar{d}_1^{\,3} - 25.783 \cdot \bar{d}_1^{\,2} + 0.3716 \cdot \bar{d}_1 + 0.5828 \tag{6}$$

In comparison to the red line in Fig. 3(a), the red line in Fig. 3(c) exhibits a sharper slope, resulting in greater changes in f_{INZ} as d_1 increases. Figs. 3(b) and 3(d) show the dispersion curves for different values of d_1 (indicated by circles in Figs. 3(a) and 3(c)). A clear decrease in the INZ frequency is observed as d_1 increases. It is also important to emphasize that, in theory, it is possible to engineer the fitting curve by designing a suitable ratio between d_1 and d_2, such as establishing a nearly linear relationship between f_{INZ} and d_1 within the range of $0.05\lambda_m < d_1 < 0.1\lambda_m$. This linear relationship could have potential applications in phase modulators, optical filters, and frequency combs.

It is well known that an INZ wave can travel with no phase shift, which provides a potential approach to building a phase modulator. By designing a joint structure that contains two one-way waveguides with the same one-way region, and if the second waveguide supports the one-way INZ mode, it is theoretically possible to control the output phase by manipulating the joint position or the lengths of the waveguides. As analyzed in Fig. 2, the EDYE structure possesses the same one-way region as the MDYE structure, and an INZ mode is present in the EDYE structure. Therefore, as shown in Fig. 4(f), we propose a novel phase modulator called the 'MDYE-EDYE' structure. We further investigate how the joint position L_x affects the output phase of the electric field (E_z). In Fig. 4(a), a clear linear relationship between the phase ($\arg(E_z)$) and L_x is observed, suggesting that such a simple structure can achieve precise phase modulation.

From Fig. 4(a), it is evident that to achieve a phase shift range of $[-\pi, \pi]$, the position shift ΔL_x should be approximately 20 mm, whereas the theoretical value in the lossless condition is around 19.3125 mm ($k \simeq 3.1068k_m$). To clearly demonstrate the linear relationship between the phase angle of E_z and L_x, we perform four full-wave simulations in a lossy condition with $\nu = 10^{-3}$, where L_x is set to 40 mm (Fig. 4(b)), 50 mm (Fig. 4(c)), 60 mm (Fig. 4(d)), and 70 mm (Fig. 4(e)). Consequently, the output E_z in Figs. 4(b) and 4(d) are both positive with nearly the same phase, as well as in Figs. 4(c) and 4(e). Therefore, it is reasonable to believe that even in a real lossy condition, our proposed 'MDYE-EDYE' structure can function as a precise all-optical phase modulator, offering advantages such as robustness against backscattering

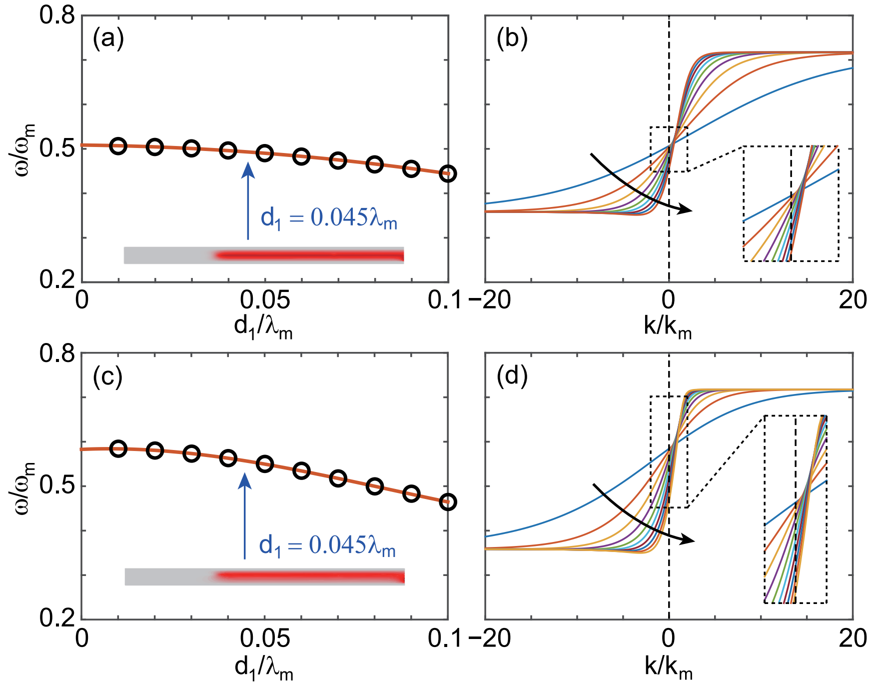

Fig. 3. The operating frequencies of INZ modes as a function of d_1 in the cases of (a) $d_1 = d_2$ and (c) $d_2 = 2d_1$. The dispersion curves of one-way SMPs as the thicknesses changing (b) in case (a), and (d) in case (c).

reflection and a straightforward manufacturing process. Compared to previous all-optical phase modulators based on Mach–Zehnder Interferometers [42,43], metasurfaces [44,45], and/or metamaterials [46], our proposed structure exhibits comparable performance and simplicity.

By employing the finite-difference time-domain (FDTD) method, the negligible effect of the loss on the INZ modes is also evident in Fig. 4(g), where a ’thick - thin - thick’ structure is designed and the INZ mode can only be sustained in the middle part. As depicted in Fig. 4(g), for the two thicker parts ($d_1 = 0.05\lambda_m$), the effective wavelengths are relatively small, while for the middle part ($d_1 = 0.03\lambda_m$), the wave is compressed (squeezing) and then travels unidirectionally through (tunneling) the section with a large wavelength at $t = 35t_r$. Consequently, we emphasize that the material loss has a relatively minor impact on the INZ modes, and altering structural parameters like air thickness can effectively mitigate this impact (not discussed here). We will further investigate the INZ-based energy squeezing and tunneling (EST) in our forthcoming work.

3. Perfect filter, all-optical splitter, and self-consistent all-optical logic gates based on INZ modes

Furthermore, through careful assembling, the remanence-based MO system can function as a perfect filter, effectively separating electromagnetic (EM) waves within a specific frequency band into two separate channels with identical bandwidth. Fig. 5(b) illustrates the Y-shaped filter, which consists of three arms. The horizontal arm serves as the input port, while the other two arms, namely the ‘EDYM’ and ‘EDYE’ structures (previously studied in the previous subsection, Figs. 1(a) and 1(b)), function as the output ports. It is important to note that the magnetization direction in the ‘EDYM’ structure has been reversed to support the forward propagation of EM waves. The input port is referred to as the ‘EYYE’ structure, with the interconnected YIG layers having opposite magnetization directions. As shown in Fig. 5(a), the ‘EYYE’ structure exhibits a significantly wide one-way region, $0 < \omega < \omega_r$, which corresponds to the combined one-way regions of the ‘EDYE’ structure ($0.5\omega_r < \omega < \omega_r$) and the ‘EDYM’ structure ($0 < \omega < 0.5\omega_r$).

Benefiting from the unique relationship between the one-way regions of the input port (‘A’) and the output ports (‘B’ and ‘C’), along with the robustness of one-way EM waves, it can be theoretically guaranteed that the excited one-way EM wave from the input port will propagate into either of the output ports. To verify the performance of the filter, we conducted two FEM simulations in this structure with frequencies set at $f = 0.5f_m$ (the second image in Fig. 5(c)) and $f = 0.2f_m$ (the third image in Fig. 5(c)). As a result, the excited wave from ‘A’ propagated to the junction point and decisively injected into either ‘B’ or ‘C’, resulting in an extremely high contrast ratio between the output ports. Therefore, the simulation results align with our theoretical analysis. It is worth noting that the phase delay within the passband is non-uniform. This non-uniformity arises because, for both the input and output sections, the wavenumbers of the guiding modes with different frequencies differ, leading to distinct coupling processes and phase shifts. A zero phase shift can only be achieved in region ‘B’ when the operating frequency is close to the INZ frequency (refer to the left simulation in Fig. 5(c)). The proposed perfect filter has the potential to serve crucial roles such as an optical switch in an integrated optical circuit. By directly changing the working frequency, the state of the communication system can be switched between ‘work’ and ‘stop’.

Besides, it is worth noting that the ‘EDYE’, ‘MDYE’, and ‘EYYE’ structures have overlapping one-way regions, but the wavenumbers of the one-way SMPs differ. As a result, one-way SMPs with different frequencies propagating in these structures will have different effective refractive indexes (n_{eff}) and may induce different splitting ratios (η). Fig. 6(c) illustrates the designed Y-shaped splitter, consisting of the ‘MDYE’ (‘A’), ‘EYYE’ (‘B’), and ‘EDYE’ (‘C’) structures. Fig. 6(a) presents the dispersion curves of SMPs in the vicinity of the overlapping one-way region ($0.5\omega_r \le \omega < \omega_r$). It is important to note that we set $d_1 = d_2 = 0.01\lambda_m$ to engineer an SMP with an infinite wavenumber at $\omega = 0.5\omega_r$ (the lower limit of the shaded region in Fig. 6(a)) in the ‘EDYE’ structure, which implies $n_{\mathrm{eff}} \to \infty$ and consequently zero transmittance in the ‘A-C’ channel should be observed under this condition. We performed FEM simulations in the designed splitter, with the frequency changing within the one-way region, and calculated the transmittance. As depicted in Fig. 6(b), the red and black lines represent the transmittance of the ‘A-B’ and ‘A-C’ channels, respectively. As expected, when $\omega = 0.5\omega_r = 0.3587\omega_m$, nearly 100% of the energy traveled through the ’A-B’ channel (as shown in the second picture in Fig. 6(c)).

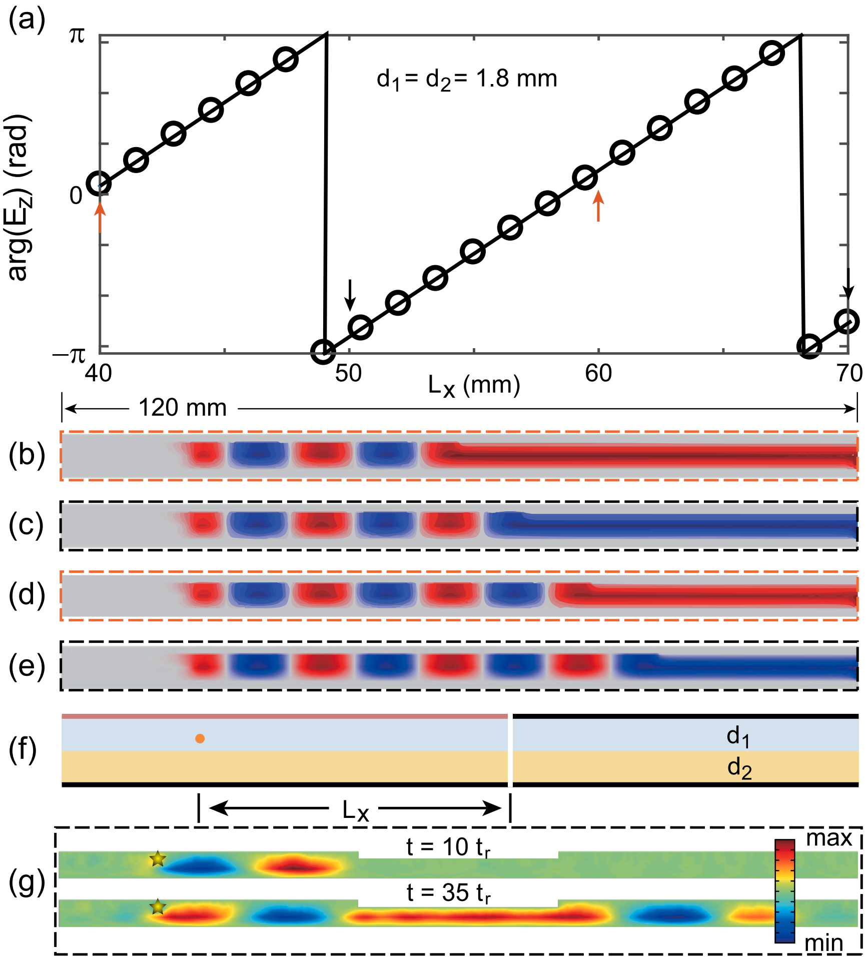

Fig. 4. All-optical phase modulator and energy squeezing and tunneling (EST) relied on INZ modes. (a) The phase angle of E_z of the output INZ modes as a function of L_x. (b)–(e) Electric filed distributions of the FEM simulations, and L_x are equal to (b) 40 mm, (c) 50 mm, (d) 60 mm, and (e) 70 mm, respectively. (f) The schematic picture of the INZ modes-based phase modulator. (g) Simulations of INZ-based EST using the FDTD method at different times with the loss factor $\nu = 10^{-3}$. $t_r = 2\pi/\omega_r$. Other parameters are $d_1 = d_2 = 0.03\lambda_m$, and $f = 0.5007 f_m$ ($f_m = 5$ GHz).

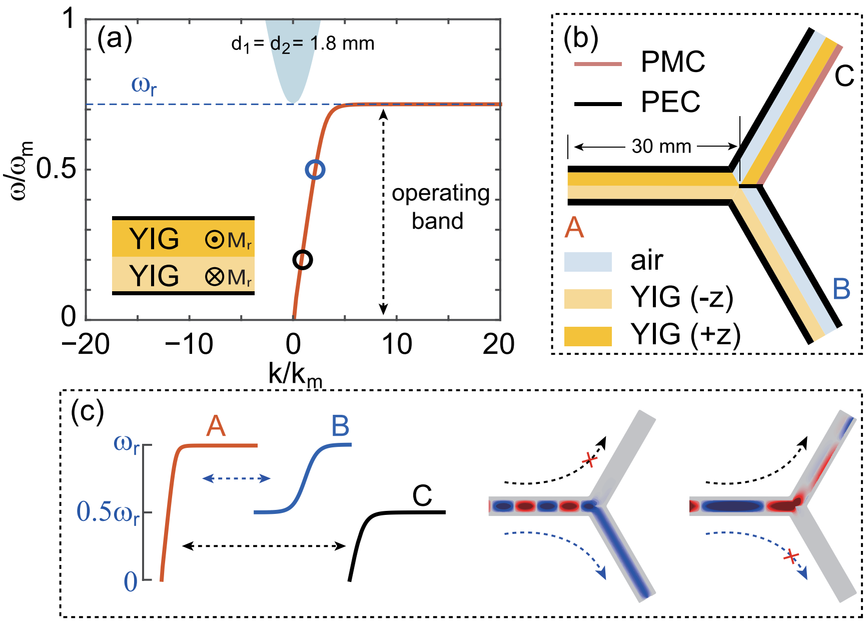

Fig. 5. (a) Dispersion diagram of the YIG-YIG structure. (b) The schematic picture and (c) simulations of the perfect optical filter with frequencies are $f = 0.5 f_m$ (marked by blue circle in (a)) and $f = 0.2 f_m$ (marked by black circle in (a)), respectively.

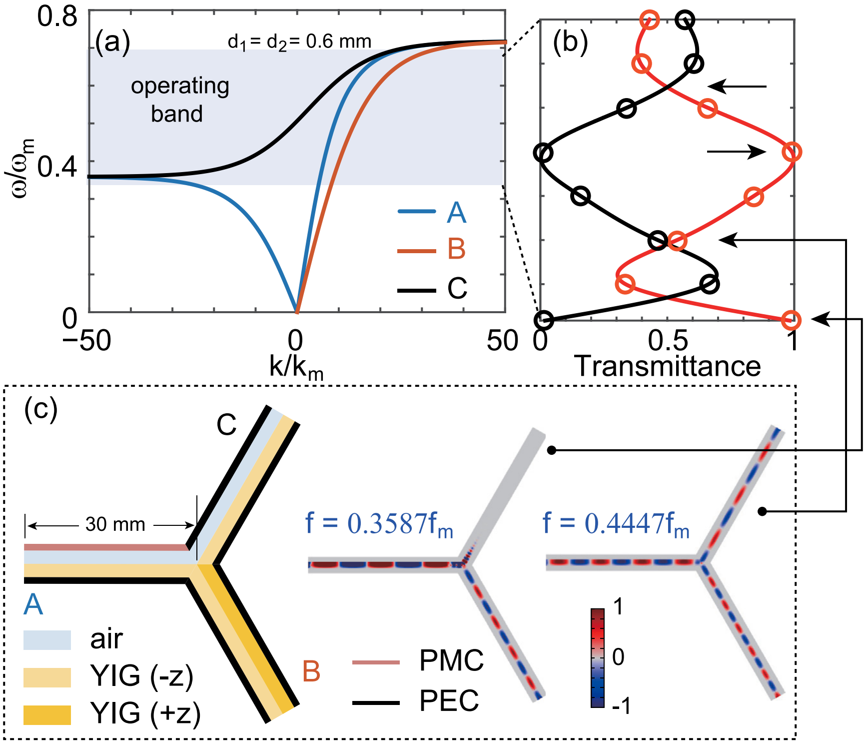

Fig. 6. (a) Dispersion diagrams of three arms of a novel tunable splitter shown in (c). (b) Relationship between transmittances of two output arms and the operating frequency within the one-way region (colored area in (a)). (c) The schematic diagram and simulations for splitting ratio $\eta = 0/100$ (second picture) and $\eta = 50/50$ (last picture). Other parameters are $d_1 = d_2 = 0.01\lambda_\mathrm{m}$ and $\nu = 10^{-3}$.

More importantly, as the frequency gradually increases to $0.4447\omega_\mathrm{m}$, the splitting ratio can approach 50/50 (as shown in the last picture in Fig. 6(c)), which is a highly desirable value in the field of optical communication. Another noteworthy case occurs when $\omega \simeq 0.45\omega_\mathrm{m}$ (indicated by the right arrow in Fig. 6(b)). In this scenario, the EM wave cannot pass through the 'A-C' channel either. This behavior can be explained by the theory of total internal reflection: (1) the effective indices of 'A', 'B', and 'C' are approximately 19.4082 ($k \simeq 10.6745k_\mathrm{m}$), 29.4398 ($k \simeq 16.1919k_\mathrm{m}$), and 6.8467 ($k \simeq 3.7657k_\mathrm{m}$), respectively; (2) the incident angle is $\pi/3$, which is clearly larger than the 'critical angle' (equal to arcsin(6.8467/19.4082)) of the 'A-C' channel.

When the frequency is further increased to approximately $0.6456\omega_\mathrm{m}$, a 50/50 splitting ratio will be achieved (indicated by the black left arrow in Fig. 6(b)). Therefore, our proposed remanence-based all-optical splitter has the capability to maintain a constant splitting ratio for different frequencies. For example, it can achieve $\eta = 50/50$ at $\omega = 0.4447\omega_\mathrm{m}$ and/or $\omega = 0.6456\omega_\mathrm{m}$, which we believe is extremely important for parallel optical computing. More importantly, the splitter proposed here can achieve a weighted splitting ratio through different methods. Firstly, depending on the operating frequency, the splitting ratio can vary from 50/50 to almost 0/100 within a frequency band (as seen in Fig. 6(b)). This characteristic holds significant potential for applications in all-optical communication and computing, especially in parallel computing. For instance, we can use the structure in Fig. 6(c) to deliver an electromagnetic wave with $f = 0.4447f_\mathrm{m}$ equally to two output ports for subsequent processing. At the same time, we can input an electromagnetic wave with $f = 0.3587f_\mathrm{m}$, allowing it to pass through only port 'B' for operations distinct from those performed with the previous frequency. Compared to traditional reciprocal splitters, this approach undoubtedly improves efficiency and reduces energy loss. Furthermore, by changing the waveguide parameters, such as the values of d_1 and d_2, the incident wave with the same frequency can be split into different splitting ratios. This characteristic of controllable splitting ratios is one of the most important features of our proposed splitter. This entails optimizing energy distribution based on the time/length that the respective signals (with distinct frequencies) necessitate. This methodology exhibits promise, especially given the continuous and relatively broad operating band, a departure from other splitter types where operating frequencies are generally discontinuous.

Recently, a possible method to achieve all-optical LGs with an extremely high contrast ratio was proposed [23]. However, there was an unresolved issue in the previously proposed LGs, which involved inconsistency between the logic of the input and output ports. In this study, we propose another Y-shaped system based on INZ modes, which can function as all-optical LGs such as OR, AND, and NAND gates. Following a consistent positive logic convention, the presence of EM energy is treated as logic '1' and is utilized in both the input and output ports, while the phase angle of E_z serves as the reference quantity in the output port. Fig. 7(a) illustrates the schematic diagram of the designed system. One can observe that this structure is very similar to the one shown in Fig. 6(c), except for the exchange of YIG layers in arm 'B'. As discussed earlier, all three arms share the same one-way region, $0.5\omega_\mathrm{r} < \omega < \omega_\mathrm{r}$. In contrast to arm 'B' shown in Fig. 6, the arm in Fig. 7 can sustain backward-propagating SMPs (as shown in the inset of Fig. 7(a)). Consequently, two one-way channels are successfully engineered based on the splitter model shown in Fig. 6. In contrast to the working frequency used in previous works, we choose the **INZ frequency** in the output port as the working frequency in order to preserve the phase information in the output section.

The proposed system can be theoretically treated as a combination of basic LGs such as OR, AND, and NAND gates. For the OR gate, we utilize positive logic, where any presence of EM energy is considered logic '1'. Based on the robust one-way channels, any input EM signal (logic '1') from either arm 'A' or arm 'B' can unidirectionally propagate through arm 'C' (also logic '1'). Hence, the system naturally functions as an OR gate.

To implement an AND gate, we introduce a reference quantity, the phase angle (θ) of E_z, to determine the state of the output port. Specifically, we assume that the output EM signal with $-\pi/2 < \theta < \pi/2$

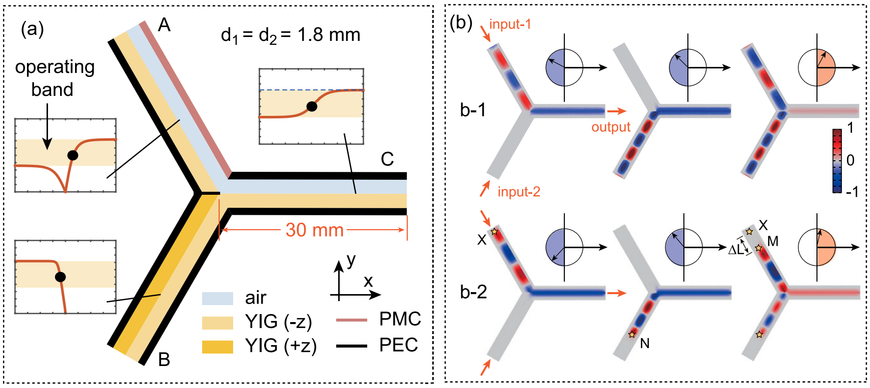

(c)

OR gate		
input-1	input-2	output
1	0	1
0	1	1
1	1	1

AND gate		
input-1	input-2	output
1	0	0
0	1	0
1	1	1

NAND gate		
input-1	input-2	output
1	0	1
0	1	1
1	1	0

Fig. 7. (a) Schematic picture of all-optical LGs based on YIG with remanence. (b) Logic operations and FEM simulations for three different inputs, i.e. ['1', '0'], ['0', '1'], and ['1', '1']. (c) The truth table for OR, AND, and NAND gates according to simulation results shown in (b).

represents logic '1'. It is important to note that the detection of electric-field phase is technically achievable by employing technologies such as scattering-type Scanning Near-field Optical Microscopy (s-SNOM) [47]. As illustrated in Fig. 7(b-1), three input combinations, ['1', '0'], ['0', '1'], and ['1', '1'], yield three corresponding outputs, logic '0', logic '0', and logic '1'. It should be noted that we set $\theta \simeq 1.4$ rad for input-1 to engineer an appropriate output phase angle. Therefore, in practical applications, the input θ needs to be tailored for different inputs. In Fig. 7(b-1), the inputs $[\theta_1, \theta_2]$ are [−1.9 rad,], [, 1.4 rad], and [1.4 rad, 1.4 rad], respectively.

The source location can indeed be optimized to engineer the appropriate input $[\theta_1, \theta_2]$, thereby enabling the realization of the proposed self-consistent LGs. For example, in Fig. 7(b-2), the input source for input-2 was fixed at point 'N' across all cases, while the source position for input-1 was shifted from point 'X' to point 'M' in the ['1', '1'] case. Based on the results presented in Fig. 7(b-1), the distance between points 'X' and 'M' can be calculated using the relation $\Delta L = \frac{\Delta\theta_1}{2\pi}\lambda_{\mathrm{eff}}$, where λ_{eff} represents the effective wavelength in input-1. This yields a value of $\Delta L \approx 10$ mm. As illustrated in Fig. 7(b-2), self-consistent LGs were successfully realized in this configuration.

Fig. 7(c) presents the truth table for the OR, AND, and NAND gates. It is evident that the outputs are inverted for the AND and NAND gates. Therefore, based on the analysis of the AND gate, the system can easily achieve NAND operation by assuming that the output EM signal with $-\pi/2 < \theta < \pi/2$ represents logic '0'. Furthermore, other basic LGs can be straightforwardly extended. With improved integration and consistent logic, the proposed Y-shaped LGs enhance the potential applications of one-way mode-based LGs in the all-optical calculation of integrated optical circuits.

The above-mentioned all-optical phase modulator, filter, and LGs, which are based on YIG with remanence, can be straightforwardly extended from 2D models to 3D structures [38]. As depicted in the inset of Fig. 8(a), two PEC walls are introduced in the z direction to confine the guided wave within the device. The simulation result shown in Fig. 8(a) exhibits similarities to the corresponding 2D case (Fig. 4(e)). Figs. 8(b)–8(d) illustrate the simulation outcomes for the 3D perfect filter, 3D splitter, and 3D LGs, respectively, and all the results are consistent with their 2D counterparts. Consequently, our proposed all-optical structures hold great potential for practical device implementation.

The theoretical findings presented in this paper are validated through simulations using the FEM and the FDTD method, both of which are well-established numerical approaches with demonstrated accuracy. Experimental validations of unidirectional functional devices involving remanence and magnetized YIG have been extensively corroborated by multiple research teams [9,39,48–50], ensuring the reproducibility of these results. The robust one-way propagation characteristics inherent in such systems further simplify practice implementation, as signal transmission remains largely unaffected by structural defects [23]. This resilience significantly reduces manufacturing complexity compared to alternative technologies.

A critical remaining challenge lies in the realization of artificial PMC walls. However, this issue may be addressed through carefully engineered high-impedance surfaces, as suggested in prior studies [49,51]. Notably, numerous complex YIG-based devices have already been successfully conceptualized and fabricated, with experimental results consistently aligning with FEM simulations [39]. Given this demonstrated track record of YIG device implementation, the functional heterostructures proposed in our work – which are characterized by their geometric simplicity – are expected to be readily realizable in experimental settings.

More importantly, as depicted in Fig. 1, our proposed all-optical phase modulator, filter, splitter, and LGs can be easily assembled on a chip. Therefore, it holds significant promise for enabling flexible all-optical computation and communication. More specifically, integrated and assembled devices offer clear advantages in reducing equipment cost and size, as well as enhancing flexibility due to their assembly capabilities. The reliability of such a system should be significantly improved since fewer inputs are needed compared to conventional optical structures. Theoretically, within a designed system depicted in Fig. 1, one can perform rich and complex optical manipulations on the input electromagnetic waves, such as optical signal modulation and demodulation, as well as optical signal distribution and consolidation. Given that the proposed devices rely on one-way propagation waves and are capable of being assembled, another evident communication application of the YIG-based structure is encoding and/or decoding the input signal by carefully designing the signal route in the system.

It is noteworthy that, through numerical simulations, we have demonstrated the high efficiency of our proposed all-optical functional devices (with L_{eff} approximately several times λ_0) at the ultra-subwavelength scale ($\sim 10^{-2}\lambda_0$). Owing to back-scattering and manufacturing defects, the values of L_{eff} for normal reciprocal all-optical

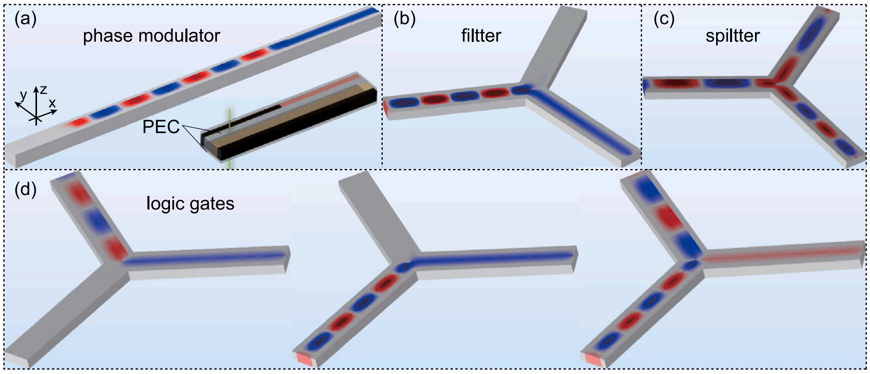

Fig. 8. Realization of 3D all-optical phase modulator, perfect filter, and self-consistent LGs.

devices are conceivably small. Furthermore, operational bands in conventional all-optical devices may be narrow or discontinuous, exemplified by resonant-based filters . In contrast, our proposed devices operate within a relatively broad and continuous band, covering either the entirety or a portion of the one-way band.

Moreover, owing to the robust unidirectional propagation characteristic, the extinction ratios (ERs) or contrast ratios (CRs) of the proposed all-optical filter and logic gates are theoretically infinite. In contrast, for most other types of filters or logic gates, ERs and/or CRs are usually smaller than 30 dB. Additionally, little research has been conducted to propose a suitable assembled unit for constructing multifunctional all-optical devices, as demonstrated in this work. This scarcity of research can be attributed to the limited connections between different functional devices. Thus, integrating a pre-designed structure with other structures to achieve different functionalities is challenging. For example, a splitter typically possesses one input and two outputs, and reassembling the input and/or output components usually cannot efficiently construct a logic gate, which necessitates two inputs and one output. The reason this approach succeeds in our proposed system is that, after reassembling, the unidirectional propagation direction in one of the arms is reversed—a feat generally unattainable in other non-unidirectional modes-based systems.

It should be noted that the multi-functional devices proposed in this paper are critically dependent on the dispersion characteristics of the output section. For instance, in the phase modulator, the operating frequency (i.e., INZ frequency) varies accordingly for distinct output structures (directly linked to dispersion curves). Similarly, in the all-optical filters, splitters, and LGs proposed here, both the structural configuration and dispersion properties of the output section govern the device's filtering performance, splitting ratio, and operational frequency. Moreover, the mechanism proposed for achieving multi-functional and assembled all-optical devices in this work is theoretically applicable to other MO structures and different regimes, such as magnetized InSb-based structures operating at terahertz frequencies. However, exploring a similar one-way band relation (as demonstrated in this work) in different arms or structures is necessary, and the heterostructures must be meticulously designed. Additionally, effects like nonlocal effects should be taken into account in such cases, especially when the wavenumber is relatively large (e.g. $k > 100k_0$).

4. Conclusion

In conclusion, we have proposed a series of all-optical devices based on YIG with remanence. The all-optical phase modulator utilizes INZ modes and allows for controllable phase modulation in a linear relationship with the length of the boundary. The INZ frequency can be adjusted by manipulating the thickness parameters, providing tunability. Moreover, we have designed a perfect filter, which separates the input port's one-way region into two parts and creates two one-way channels with equal bandwidth. Additionally, we have introduced an all-optical splitter that divides the input wave into two output ports with a customizable and precise splitting ratio, such as 50/50. Furthermore, we have proposed all-optical logic gates based on one-way INZ modes, where the phase angle of the output signal are used to determine the logic states. Basic logic gates, including OR, AND, and NAND, have been achieved based on this principle. The feasibility and performance of the proposed devices have been validated in both 2D and 3D simulations. Our proposed multi-functional all-optical devices hold potential for optical calculations, including parallel computing in integrated optical circuits.

CRediT authorship contribution statement

Jie Xu: Writing – original draft, Visualization, Conceptualization. **Yun You:** Writing – review & editing, Visualization. **Sanshui Xiao:** Writing – review & editing, Visualization. **Lujun Hong:** Writing – review & editing. **Yun Shen:** Writing – review & editing. **Kosmas L. Tsakmakidis:** Writing – review & editing, Supervision, Conceptualization. **Yamei Luo:** Writing – review & editing, Supervision.

Declaration of competing interest

The authors declare that they have no known competing financial interests or personal relationships that could have appeared to influence the work reported in this paper.

Acknowledgments

This work was supported by the National Natural Science Foundation of China (NSFC) (No. 12404143, No. 62101496), the Natural Science Foundation of Sichuan Province (No. 2023NSFSC1309), Program of Luzhou Science and Technology bureau (No. 2023JYJ046, No. 2023JYJ032), and the General Secretariat for Research and Technology (GSRT) and the Hellenic Foundation for Research and Innovation (HFRI) under Grant No. 4509.

Appendix A. Supplementary data

Supplementary material related to this article can be found online at https://doi.org/10.1016/j.optlastec.2025.112858.

Data availability

No data was used for the research described in the article.

References

[1] L. Tong, R.R. Gattass, J.B. Ashcom, S. He, J. Lou, M. Shen, I. Maxwell, E. Mazur, Subwavelength-diameter silica wires for low-loss optical wave guiding, Nature 426 (6968) (2003) 816–819.

[2] J. Feldmann, N. Youngblood, M. Karpov, H. Gehring, X. Li, M. Stappers, M. Le Gallo, X. Fu, A. Lukashchuk, A.S. Raja, J. Liu, C.D. Wright, A. Sebastian, T.J. Kippenberg, W.H.P. Pernice, H. Bhaskaran, Parallel convolutional processing using an integrated photonic tensor core, Nature 589 (7840) (2021) 52–58.

[3] R. Zhuang, K. Ni, G. Wu, T. Hao, L. Lu, Y. Li, Q. Zhou, Electro-optic frequency combs: Theory, characteristics, and applications, Laser & Photonics Rev. 17 (2023) 2200353.

[4] V.V. Vogler-Neuling, A. Karvounis, A. Morandi, H. Weigand, E. Dénervaud, R. Grange, Photonic assemblies of randomly oriented nanocrystals for engineered nonlinear and electro-optic effects, ACS Photonics 9 (7) (2022) 2193–2203.

[5] X. Chen, J. Lin, K. Wang, A review of silicon-based integrated optical switches, Laser & Photonics Rev. 17 (4) (2023) 2200571.

[6] M. Ren, W. Cai, J. Xu, Tailorable dynamics in nonlinear optical metasurfaces, Adv. Mater. 32 (3) (2020) 1806317.

[7] J. Xu, X. Deng, H. Zhang, C. Wu, M. Wubs, S. Xiao, L. Shen, Ultra-subwavelength focusing and giant magnetic-field enhancement in a low-loss one-way waveguide based on remanence, J. Opt. 22 (2) (2020) 025003.

[8] K.L. Tsakmakidis, L. Shen, S.A. Schulz, X. Zheng, J. Upham, X. Deng, H. Altug, A.F. Vakakis, R.W. Boyd, Breaking lorentz reciprocity to overcome the time-bandwidth limit in physics and engineering, Science 356 (6344) (2017) 1260–1264, http://dx.doi.org/10.1126/science.aam6662.

[9] S. Li, K.L. Tsakmakidis, T. Jiang, Q. Shen, H. Zhang, J. Yan, S. Sun, L. Shen, Unidirectional guided-wave-driven metasurfaces for arbitrary wavefront control, Nat. Commun. 15 (1) (2024) 5992, http://dx.doi.org/10.1038/s41467-024-50287-z.

[10] F. Zangeneh-Nejad, D.L. Sounas, A. Alù, R. Fleury, Analogue computing with metamaterials, Nat. Rev. Mater. 6 (3) (2021) 207–225.

[11] G.-J. Tang, X.-T. He, F.-L. Shi, J.-W. Liu, X.-D. Chen, J.-W. Dong, Topological photonic crystals: physics, designs, and applications, Laser & Photonics Rev. 16 (4) (2022) 2100300.

[12] G. Ma, M. Xiao, C.T. Chan, Topological phases in acoustic and mechanical systems, Nat. Rev. Phys. 1 (4) (2019) 281–294.

[13] Y. Poo, R. x. Wu, Z. Lin, Y. Yang, C.T. Chan, Experimental realization of self-guiding unidirectional electromagnetic edge states, Phys. Rev. Lett. 106 (9) (2011) 093903.

[14] P. Zhou, G.-G. Liu, X. Ren, Y. Yang, H. Xue, L. Bi, L. Deng, Y. Chong, B. Zhang, Photonic amorphous topological insulator, Light: Sci. Appl. 9 (1) (2020) 133.

[15] M. Wang, R.-Y. Zhang, L. Zhang, D. Wang, Q. Guo, Z.-Q. Zhang, C.T. Chan, Topological one-way large-area waveguide states in magnetic photonic crystals, Phys. Rev. Lett. 126 (6) (2021) 067401, http://dx.doi.org/10.1103/PhysRevLett.126.067401.

[16] S.A. Skirlo, L. Lu, Y. Igarashi, Q. Yan, J. Joannopoulos, M. Soljačić, Experimental observation of large chern numbers in photonic crystals, Phys. Rev. Lett. 115 (25) (2015) 253901, http://dx.doi.org/10.1103/physrevlett.115.253901.

[17] L. Maigyte, K. Staliunas, Spatial filtering with photonic crystals, Appl. Phys. Rev. 2 (1) (2015) 011102.

[18] S. Ma, B. Xiao, Y. Yu, K. Lai, G. Shvets, S.M. Anlage, Topologically protected photonic modes in composite quantum hall/quantum spin hall waveguides, Phys. Rev. B 100 (8) (2019) 085118.

[19] X. Guo, Y. Ding, Y. Duan, X. Ni, Nonreciprocal metasurface with space–time phase modulation, Light: Sci. Appl. 8 (1) (2019) 123.

[20] J. Xu, P. He, D. Feng, K. Yong, L. Hong, Y. Shen, Y. Zhou, Slow wave and truly rainbow trapping in a one-way terahertz waveguide, Opt. Express 29 (7) (2021) 11328–11341, http://dx.doi.org/10.1364/OE.422274.

[21] J. Xu, Q. Shen, K. Yuan, X. Deng, Y. Shen, H. Zhang, C. Wu, S. Xiao, L. Shen, Trapping and releasing bidirectional rainbow at terahertz frequencies, Opt. Commun. 473 (2020) 125999, http://dx.doi.org/10.1016/j.optcom.2020.125999.

[22] Y. Zhou, P. He, S. Xiao, F. Kang, L. Hong, Y. Shen, Y. Luo, J. Xu, Realization of tunable index-near-zero modes in nonreciprocal magneto-optical heterostructures, Opt. Express 30 (15) (2022) 27259–27272.

[23] J. Xu, F. Kang, Y. Luo, S. Xiao, K.L. Tsakmakidis, All-optical digital logic based on unidirectional modes, Adv. Opt. Mater. 11 (1) (2023) 2201836, http://dx.doi.org/10.1002/adom.202201836.

[24] S.A.H. Gangaraj, F. Monticone, Do truly unidirectional surface plasmon-polaritons exist? Optica 6 (9) (2019) 1158–1165.

[25] K.L. Tsakmakidis, K. Baskourelos, T. Stefański, Topological, and nonreciprocal, and multiresonant slow light beyond the time-bandwidth limit, Appl. Phys. Lett. 119 (19) (2021) 190501, http://dx.doi.org/10.1063/5.0068285.

[26] J. Brion, R. Wallis, A. Hartstein, E. Burstein, Theory of surface magnetoplasmons in semiconductors, Phys. Rev. Lett. 28 (22) (1972) 1455, http://dx.doi.org/10.1103/PhysRevLett.28.1455.

[27] Y. Zhou, M.Z. Alam, M. Karimi, J. Upham, O. Reshef, C. Liu, A.E. Willner, R.W. Boyd, Broadband frequency translation through time refraction in an epsilon-near-zero material, Nat. Commun. 11 (1) (2020) 1–7.

[28] X. Niu, X. Hu, S. Chu, Q. Gong, Epsilon-near-zero photonics: a new platform for integrated devices, Adv. Opt. Mater. 6 (10) (2018) 1701292.

[29] M. Silveirinha, N. Engheta, Tunneling of electromagnetic energy through sub-wavelength channels and bends using ϵ -near-zero materials, Phys. Rev. Lett. 97 (15) (2006) 157403, http://dx.doi.org/10.1103/physrevlett.97.157403, https://link.aps.org/doi/10.1103/PhysRevLett.97.157403.

[30] J.S. Marcos, M.G. Silveirinha, N. Engheta, μ -near-zero supercoupling, Phys. Rev. B 91 (19) (2015) 195112.

[31] A.M. Mahmoud, N. Engheta, Wave–matter interactions in epsilon-and-mu-near-zero structures, Nat. Commun. 5 (1) (2014) 5638.

[32] T. Fakhrul, S. Tazlaru, L. Beran, Y. Zhang, M. Veis, C.A. Ross, Magneto-optical bi:YIG films with high figure of merit for nonreciprocal photonics, Adv. Opt. Mater. 7 (13) (2019) 1900056, http://dx.doi.org/10.1002/adom.201900056.

[33] J. Liang, Y. Li, T. Dai, Y. Zhang, X. Zhang, H. Liu, P. Wang, On-chip Ce:YIG/Si mach–Zehnder optical isolator with low power consumption, Opt. Express 31 (5) (2023) 8375–8383, http://dx.doi.org/10.1364/OE.482805.

[34] M. Popov, Y. Xiong, I. Zavislyak, H. Chumak, O. Fedorchuk, S. Saha, R. Bidthanapally, H. Qu, M.R. Page, G. Srinivasan, Y-type hexagonal ferrite-based band-pass filter with dual magnetic and electric field tunability, Sci. Rep. 13 (1) (2023) 1179.

[35] E. Almpanis, G.P. Zouros, P.A. Pantazopoulos, K.L. Tsakmakidis, N. Papanikolaou, N. Stefanou, Spherical optomagnonic microresonators: Triple-resonant photon transitions between Zeeman-split Mie modes, Phys. Rev. B 101 (5) (2020) 054412, http://dx.doi.org/10.1103/PhysRevB.101.054412.

[36] C.A. Balanis, Advanced Engineering Electromagnetics, John Wiley & Sons, 2012.

[37] Q. Shen, X. Zheng, H. Zhang, Y. You, L. Shen, Large-area unidirectional surface magnetoplasmons using uniaxial -near-zero material, Opt. Lett. 46 (23) (2021) 5978, http://dx.doi.org/10.1364/ol.444752.

[38] L. Hong, Y. Wang, Y. Shen, X. Deng, K. Yuan, S. Xiao, J. Xu, Broadband energy squeezing and tunneling based on unidirectional modes, Opt. Mater. Express 11 (9) (2021) 2975–2984, http://dx.doi.org/10.1364/ome.437468.

[39] G.-G. Liu, Z. Gao, Q. Wang, X. Xi, Y.-H. Hu, M. Wang, C. Liu, X. Lin, L. Deng, S.A. Yang, P. Zhou, Y. Yang, Y. Chong, B. Zhang, Topological Chern vectors in three-dimensional photonic crystals, Nature 609 (7929) (2022) 925–930, http://dx.doi.org/10.1038/s41586-022-05077-2.

[40] D.M. Pozar, Microwave Engineering, John Wiley & Sons, 2011.

[41] E. Baños-López, C. Cortés-Escobedo, F. Sánchez-De Jesús, A. Barba-Pingarrón, A. Bolarín-Miró, Crystal structure and magnetic properties of cerium-doped yig: Effect of doping concentration and annealing temperature, J. Alloys Compd. 730 (2018) 127–134.

[42] C. Sturm, D. Tanese, H. Nguyen, H. Flayac, E. Galopin, A. Lemaître, I. Sagnes, D. Solnyshkov, A. Amo, G. Malpuech, J. Bloch, All-optical phase modulation in a cavity-polariton Mach–Zehnder interferometer, Nat. Commun. 5 (1) (2014) 3278, http://dx.doi.org/10.1038/ncomms4278.

[43] C. Zhang, P.A. Morton, J.B. Khurgin, J.D. Peters, J.E. Bowers, Ultralinear heterogeneously integrated ring-assisted Mach–Zehnder interferometer modulator on silicon, Optica 3 (12) (2016) 1483.

[44] Z. Miao, Q. Wu, X. Li, Q. He, K. Ding, Z. An, Y. Zhang, L. Zhou, Widely tunable terahertz phase modulation with gate-controlled graphene metasurfaces, Phys. Rev. X 5 (4) (2015) 041027.

[45] W. Yang, J. Qin, J. Long, W. Yan, Y. Yang, C. Li, E. Li, J. Hu, L. Deng, Q. Du, L. Bi, A self-biased non-reciprocal magnetic metasurface for bidirectional phase modulation, Nat. Electron. 6 (3) (2023) 225–234.

[46] S. Lee, S. Baek, T.-T. Kim, H. Cho, S. Lee, J.-H. Kang, B. Min, Metamaterials for enhanced optical responses and their application to active control of terahertz waves, Adv. Mater. 32 (35) (2020) 2000250.

[47] L.N. Casses, K.J. Kaltenecker, S. Xiao, M. Wubs, N. Stenger, Quantitative near-field characterization of surface plasmon polaritons on monocrystalline gold platelets, Opt. Express 30 (7) (2022) 11181–11191, http://dx.doi.org/10.1364/OE.454740.

[48] W. Tong, J. Wang, J. Wang, Z. Liu, Y. Pang, S. Qu, Magnetically tunable unidirectional waveguide based on magnetic photonic crystals, Appl. Phys. Lett. 109 (5) (2016) 053502, http://dx.doi.org/10.1063/1.4960196.

[49] X. Huang, Y. Lai, Z.H. Hang, H. Zheng, C.T. Chan, Dirac cones induced by accidental degeneracy in photonic crystals and zero-refractive-index materials, Nat. Mater. 10 (8) (2011) 582–586, http://dx.doi.org/10.1038/nmat3030.

[50] Z. Wang, Y. Chong, J.D. Joannopoulos, M. Soljačić, Observation of unidirectional backscattering-immune topological electromagnetic states, Nature 461 (7265) (2009) 772–775, http://dx.doi.org/10.1038/nature08293.

[51] D. Dancila, X. Rottenberg, N. Focant, H.A. Tilmans, W. De Raedt, I. Huynen, Compact cavity resonators using high impedance surfaces, Appl. Phys. A 103 (2011) 799–804, http://dx.doi.org/10.1007/s00339-010-6235-6.